Science Bulletin 63 (2018) 433–440

Contents lists available at ScienceDirect

Science Bulletin

journal homepage: www.elsevier.com/locate/scib

Science Bulletin
www.scibull.com

Article

Decorating carbon nanofibers with Mo_2C nanoparticles towards hierarchically porous and highly catalytic cathode for high-performance Li-O_2 batteries

Zhen-Dong Yang [a,b], Zhi-Wen Chang [b], Qi Zhang [b,c], Keke Huang [d,*], Xin-Bo Zhang [b,*]

[a] Key Laboratory of Automobile Materials, Ministry of Education, Department of Materials Science and Engineering, Jilin University, Changchun 130022, China
[b] State Key Laboratory of Rare Earth Resource Utilization, Changchun Institute of Applied Chemistry, Chinese Academy of Sciences, Changchun 130022, China
[c] Hunan Key Laboratory for Micro-Nano Energy Materials and Device, Xiangtan University, Xiangtan 411105, China
[d] State Key Laboratory of Inorganic Synthesis & Preparative Chemistry, Jilin University, Changchun 130022, China

ARTICLE INFO

Article history:
Received 30 November 2017
Received in revised form 7 February 2018
Accepted 7 February 2018
Available online 13 February 2018

Keywords:
Li-O_2 battery
Carbon nanofibers film
Mo_2C nanoparticles
Electrospinning
Binder-free

ABSTRACT

A facile synthesis of the hierarchically porous cathode with Mo_2C nanoparticles through the electrospinning technique and heat treatment is proposed. The carbonization temperature of the precursors is the key factor for the formation of Mo_2C nanoparticles on the carbon nanofibers (MCNFs). Compared with the Mo_2N nanoparticles embedded into N-doped carbon nanofibers film (MNNFs) and N-doped carbon nanofibers film (NFs), the battery with MCNFs cathode is capable of operation with a high-capacity (10,509 mAh g^{-1} at 100 mA g^{-1}), a much reduced discharge-charge voltage gap, and a long-term life (124 cycles at 200 mA g^{-1} with a specific capacity limit of 500 mAh g^{-1}). These excellent performances are derived from the synergy of the following advantageous factors: (1) the hierarchically self-standing and binder-free structure of MCNFs could ensure the high diffusion flux of Li^+ and O_2 as well as avoid clogging of the discharge product, bulk Li_2O_2; (2) the well dispersed Mo_2C nanoparticles not only afford rich active sites, but also facilitate the electronic transfer for catalysis.

1. Introduction

The development of electric vehicle is an effective measure to resolve the increasing environmental concerns. As one of important parts of electric vehicles (EVs), the insufficient storage capacity of current batteries is the major technical hurdle that limits the range of practical EVs. Rechargeable lithium-oxygen (Li-O_2) battery has the potential to power EVs, enabling driving ranges comparable to gasoline powered automobiles, due to its high theoretical energy density (3,600 Wh kg^{-1}) [1–6]. However, the practical use of Li-O_2 battery has been restricted by some scientific and technical challenges. First, the irregular precipitation insoluble discharge product, lithium peroxide (Li_2O_2), will block the void of the O_2 cathode [7–10]. Second, the sluggish kinetics of the oxygen reduction reaction (ORR) and the oxygen evolution reaction (OER) will seriously limit the battery performance, causing high discharge-charge overpotential, low round-trip efficiency, poor rate capability, and especially short cycle life [11,12]. Third, the commonly used organic binders, such as polyvinylidene fluoride (PVDF), will survive nucleophilic attack of high-sensitive intermediated radicals and produce unwanted products such as LiF, LiOH, and Li_2CO_3 [13–15]. Furthermore, the addition of an organic binder will inevitably increase the impedance of the cell and block the diffusion channel of Li^+ and O_2. To resolve these above problems, a hierarchically self-standing and binder-free cathode with effective catalytic performance should be designed and fabricated.

Herein, a self-standing nitrogen-doped carbon nanofibers (NFs) substrate is created by electrospinning technique. NFs could be directly used for a cathode in Li-O_2 battery because its open macroporous structure allows for the diffusion of electrolyte and O_2, provides sufficient active surface area for the cathode reactions as well as necessary pore volume for the storage of discharge products. Besides, it could eliminate the side-reactions causing by binders [16–19]. Moreover, nitrogen-doping not only increases the electrical conductivity, but also shows catalytic activities for ORR and OER [20–23]. Cathodes consisting noble metals (Pt, Au and Ru) and metal oxides (RuO_2 and IrO_2), usually exhibit much great electrochemistry performance in the Li-O_2 battery, including low

* Corresponding authors.
E-mail addresses: kkhuang@jlu.edu.cn (K. Huang), xbzhang@ciac.ac.cn (X.-B. Zhang).

https://doi.org/10.1016/j.scib.2018.02.014
2095-9273/

overpotential and high cycling stability [24–28]. However, the high cost and scarcity of noble metals terribly impede their widespread applications. What's worse, the synthesis strategies for those hybrid materials involve multiple steps and require high energy conditions and toxic/erosive reagents (such as HF or NaOH). Hence, alternative routes for the synthesis of low-cost powerful cathodes are desired. Recently, Mo_2C is believed to be as a favourable alternative of noble metals due to its Pt-like structure [29,30]. Here, Mo_2C nanoparticles are well dispersed on the NFs with controlled particle size (5–8 nm) by carbonizing polymer precursor containing molybdenum acetylacetonate at Ar/H_2 (denoted as MCNFs). It is worth noting that the carbonization temperature is the key factor to synthesize Mo_2C. Eventually, the Li-O_2 battery with MCNFs cathode shows a relatively low discharge-charge gap voltage, a large specific capacity, and a good cycling stability. These superior properties can be explained by the hierarchically self-standing and binder-free structure that could ensure the high diffusion flux of Li^+ and O_2 as well as avoid clogging of the discharge product, bulk Li_2O_2. Simultaneously, the well dispersed Mo_2C nanoparticles not only afford rich active sites, but also facilitate the electronic transfer for catalysis.

2. Materials and methods

2.1. Preparation for the cathode material

2.1.1. Chemicals

Polyacrylonitrile (M_w = 150,000, PAN) is purchased from J&K Co. Molybdenum acetylacetonate (97%, $Mo(acac)_4$) is purchased from Aladdin Reagent. *N*,*N*-dimethylformanide (99.5%, DMF), tretraethylene glycol dimethyl ether (99%, TEGDME), lithium triflate (98%, $LiCF_3SO_3$) is purchased from Macklin Reagent. All chemicals are used as received without further purification.

2.1.2. Synthesis of MCNFs

MCNFs is fabricated in a large-scale quantity via an electrospinning technique followed by anneal treatment. Typically, 1 g PAN and 0.50 g $Mo(acac)_4$ are dissolved in 5 mL DMF with vigorous stirring for 5 h. After that, the above mixture is transferred to a plastic syringe equipped with a 9-gauge metal nozzle made of stainless steel. The distance between the needle tip and the collector is fixed to 16 cm and the flow rate of the syringe pump is fixed at 1.0 mL h^{-1}. Electrospinning experiments are performed when relative air humidity is 50%–60%. The voltage is conducted at 20 kV and a sprayed dense web of fibers is collected on the aluminum foil. The electrospun polymer nanofibers first are stabilized at 280 °C for 2 h at a heating rate of 1 °C min^{-1} in air and then are carbonized at 900 °C for 6 h under Ar/H_2 (95%:5%) atmosphere to obtain MCNFs.

2.1.3. Synthesis of MNNFs

The MNNFs is synthesized by the same method as the MCNFs except the only difference that carbonization temperature is at 800 °C.

2.1.4. Synthesis of NFs

The NFs is synthesized by the same method as the MCNFs without $Mo(acac)_4$ addition.

2.2. Characterization of material

Scanning electron microscopy (SEM) analysis and energy dispersive spectroscopy (EDS) are performed using a field emission scanning electron microanalyzer (Hitachi S4800) operated at an accelerating voltage of 10 kV. Transmission electron microscopy (TEM) is performed on an FEI Tecnai G2 S-Twin instrument with a field emission gun operating at 200 kV. Powder X-ray diffraction (XRD) measurements are carried out using a Bruker D8 Focus powder X-ray diffractometer with Cu Kα (λ = 0.15405 nm) radiation (40 kV, 40 mA). X-ray photoelectron spectroscopy (XPS) analyses are conducted on a VG Scientific ESCALAB MKII X-ray photoelectron spectrometer using an Al Kα source. Thermogravimetric analysis (TGA) was performed under air atmosphere from 25 to 800 °C at a heating rate of 10 °C min^{-1} on a NETZSCH STA 449 F3 Simultaneous TGA-DSC Instrument.

2.3. Electrolytes

Tetraethylene glycol dimethyl ether (TEGDME) solvent are soaked in activated molecular sieves (4 Å type) for 30 d until the water content below 10 mg L^{-1}. $LiCF_3SO_3$ is heated at 80 °C in vacuum oven for 24 h. The electrolyte contains 1 mol L^{-1} $LiCF_3SO_3$ in TEGDME solvent (H_2O <10 ppm).

2.4. Li-O_2 cell preparation and electrochemical measurements

All the MCNFs, MNNFs, and NFs are cut into slices with a diameter of 12 mm, which are used directly as cathode without any binders. All cathodes are dried at 80 °C in vacuum oven for 24 h with the average mass being (0.50 ± 0.05) mg. The electrochemical performance of the Li-O_2 cell is analyzed using a 2025-type coin cell. All of the cells are assembled in a glove box under an Ar atmosphere using a lithium metal foil anode, a glass fiber separator, an oxygen cathode and an electrolyte containing 1 mol L^{-1} $LiCF_3SO_3$ in TEGDME. The galvanostatic discharge/charge tests are performed in a specific capacity-controlled mode at various current densities. CVs are also performed at a scan rate of 0.1 mV s^{-1} in the range of 2.0–4.5 V.

3. Results

3.1. Structures and characterizations

Fig. 1a schematically illustrates the synthesis strategy for MCNFs. First, the self-standing polymer fibers film is obtained by the electrospinning technology (Fig. S1a online). Then, the polymer fibers film is stabilized in air at 280 °C to form a ladder structure consisting of a series of connected C—N aromatic rings by the dehydrogenation and cyclization process, this ladder structure could be maintained even at high temperatures [31]. After that, the film is carbonized at 900 °C to obtain MCNFs. Interestingly, when the carbonization temperature is 800 °C, the product is that Mo_2N nanoparticles dispersed on NFs (denoted as MNNFs). MCNFs and MNNFs are both characterized using XRD as shown in Fig. 1b. The peaks of crystalline Mo_2C (JCPDS No. 65-8766) and crystalline Mo_2N (JCPDS No. 25-1366) respectively appear in broad humps in the 10°–80° range. This result confirms that Mo_2C and Mo_2N are successfully fabricated after carbonization. As we all know, the nitrogen content of PAN is about 26.4% and the electronegativity of the N atom is larger than that of C atom, the N atom is preferentially bonded with the Mo atom to form Mo_2N, so Mo_2N is first formed at low temperature. But as the temperature increases, the N atoms are eliminated and the product begins to convert from Mo_2N to Mo_2C. TGA of the precursor under Ar is shown in Fig. S2 (online). It is obviously note that there is a weight loss between 800 and 900 °C, in which prove this above conjecture.

As shown in Fig. 1c and Fig. S3a (online), the obtained MCNFs and MNNFs maintain the hierarchically self-standing and binder-free network structure even at high temperature. The average diameter of MCNFs and MNNFs is ca. 400 nm (Fig. 1c and

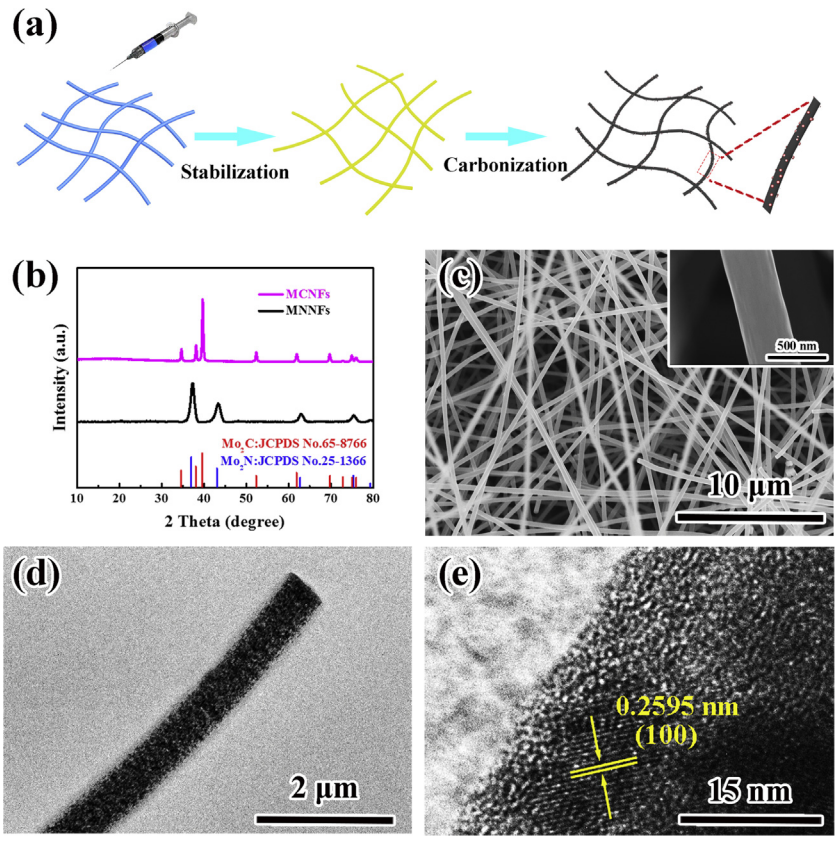

Fig. 1. (Color online) Scheme for fabrication and structure of the cathode. (a) Schematic representations for the design and preparation of MCNFs. (b) XRD patterns of the MCNFs and MNNFs. Low (c) and high (inset) resolution SEM images of MCNFs. TEM (d) and HRTEM (e) of MCNFs.

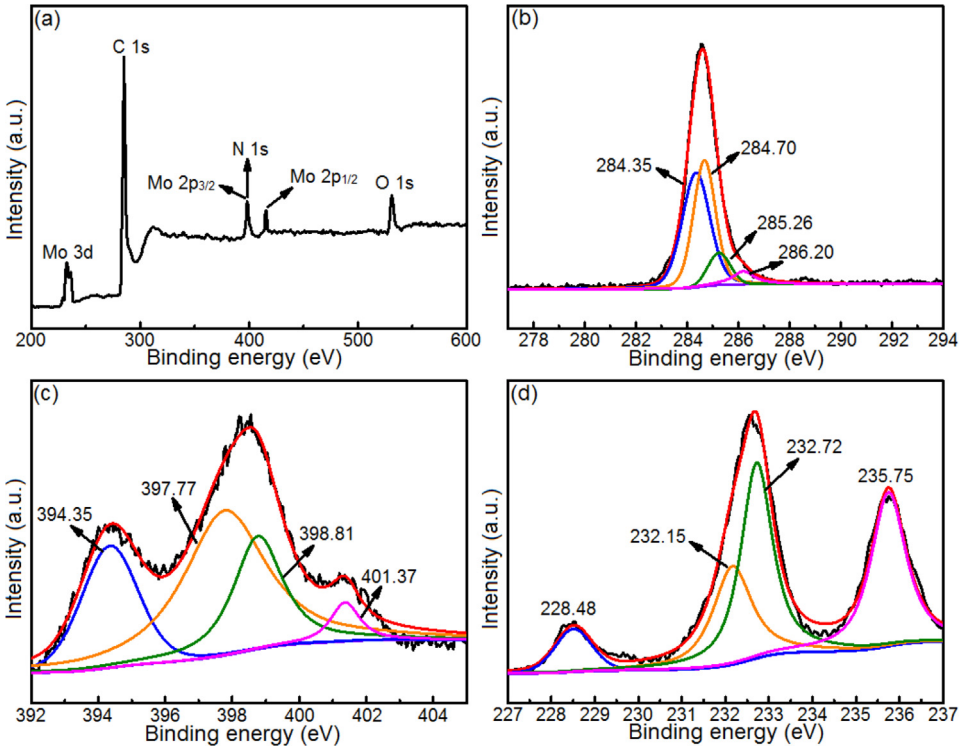

Fig. 2. (Color online) XPS spectra of the MCNFs cathode. Survey spectrum (a) and high-resolution spectra of C 1s (b), N 1s (c) and Mo 3d (d).

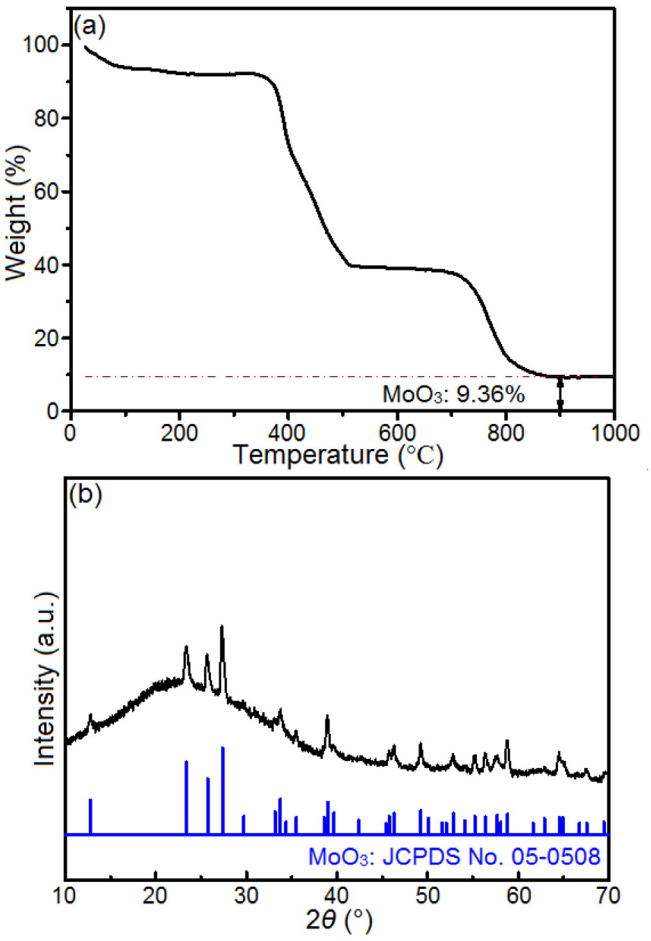

Fig. 3. (Color online) The thermal analysis of MCNFs. (a) Thermal analysis of MCNFs in the 20–1,000 °C temperature window, using a heating ramp of 10 °C min^{-1} under N_2/O_2. (b) XRD pattern of the remaining product after the thermal analysis of MCNFs.

Fig. S2b (online)), which is smaller than that before the polymer fibers film (Fig. S1b online) [32]. Interestingly, the average diameter of MCNFs and MNNFs are larger than that of NFs (Fig. S4b online). This can be explained by the viscosity of the precursor solution increasing after the addition of $Mo(acac)_4$, and the diameter of fibers increases with the increase of the viscosity [33]. As shown in Fig. 1d, a lot of nanoparticles with the size range from 5 to 10 nm are well dispersed in the carbon fibers and the d-spacing of these nanoparticles is found to be 0.2595 nm (Fig. 1e), corresponding to the (1 0 0) plane of Mo_2C (Fig. 1b).

XPS is also used to analyze the surface compositions of the MCNFs. As depicted in the survey of MCNFs, six distinct signals at 231.5, 285.0, 398.5, 400.0, 416.0 and 532.5 eV can be well ascribed to Mo 3d, C 1s, Mo $3p_{3/2}$, N 1s, Mo $3p_{1/2}$ and O 1s, respectively (Fig. 2a). Fig. 2b shows the C 1 s high spectrum, in which the peak at the lower binding energy of 284.35 eV is characteristic of the carbon in Mo_2C, whereas those at higher binding energies of 284.70, 285.26, 286.20 eV correspond to C—C, C = N, and C—N, respectively. In Fig. 2c, the N 1 s high resolution XPS spectrum presents four peaks, in which could be ascribed to Mo_2N (394.35 eV), pyridinic-N (397.77 eV), pyrrolic-N (398.81 eV) and graphitic-N (401.37 eV). Finally, the high resolution Mo 3d XPS spectrum could be deconvoluted into four peaks (Fig. 2d). The peaks at 228.48 and 232.72 eV can be assigned to Mo_2C, while the other two at 232.15 and 235.75 eV are related to the intermediate oxidation states of Mo (MoO_x). MoO_x mainly stems from the exposure of Mo_2C to air or the surface oxidation during the XPS test procedure [29,34]. TGA is applied to analyze the proportion of Mo_2C in MCNFs (Fig. 3a). The remaining product is pure phase MoO_3 after heat treatments of MCNFs (Fig. 3c). According to the molecular weight of MoO_3 and Mo_2C, we can calculate that the proportion of Mo_2C in MCNFs is 13.26%.

3.2. Electrochemical performances

The electrochemical properties of the MCNFs cathode are then examined in a Li-O_2 cell. The MNNFs and NFs are employed for comparison. Fig. 4a shows the first discharge-charge voltage profiles of the Li-O_2 cells with the MCNFs, MNNFs, and NFs cathodes at a current density of 200 mA g^{-1}. The discharge/charge voltage gap of the MCNFs is about 1.0 V, which is much lower than that of MNNFs (1.73 V) and NFs (1.90 V). Note that the discharge and charge voltage of the Li-O_2 cells can be significantly improved with the help of MCNFs cathode, which enhances the round-trip efficiency that is vital for electrochemical energy storage devices. In detail, the discharge voltage of the Li-O_2 cells with a MCNFs cathode is higher than that with MNNFs and NFs cathodes by ~30 mV; its charge voltage is much lower than that with the MNNFs cathode by 140 mV and that with the NFs cathode by 200 mV. The electrochemical processes of oxygen in the Li-O_2 cell were also investigated using cyclic voltammetry (CV) cells at a constant scan rate of 0.1 mV s^{-1}. As revealed in Fig. 4b, the ORR peak (2.37 V) of MCNFs is similar with that of MNNFs and NFs, but the onset

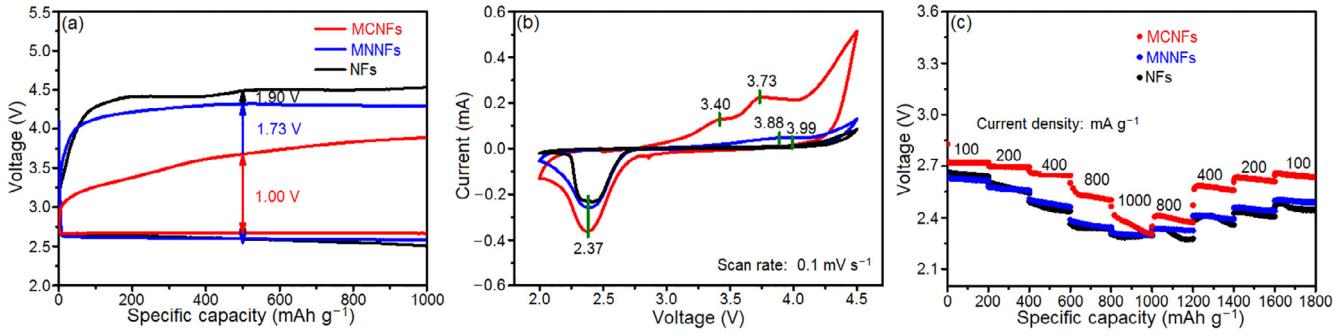

Fig. 4. (Color online) Electrochemical performance. (a) First discharge-charge curves of the Li-O_2 battery with three different cathodes at a current density of 200 mA g^{-1}; (b) CV profiles of the Li-O_2 battery with three different cathodes at voltage sweep rate of 0.1 mV s^{-1}; (c) the rate capability of the Li-O_2 batteries with three different cathodes at different current densities.

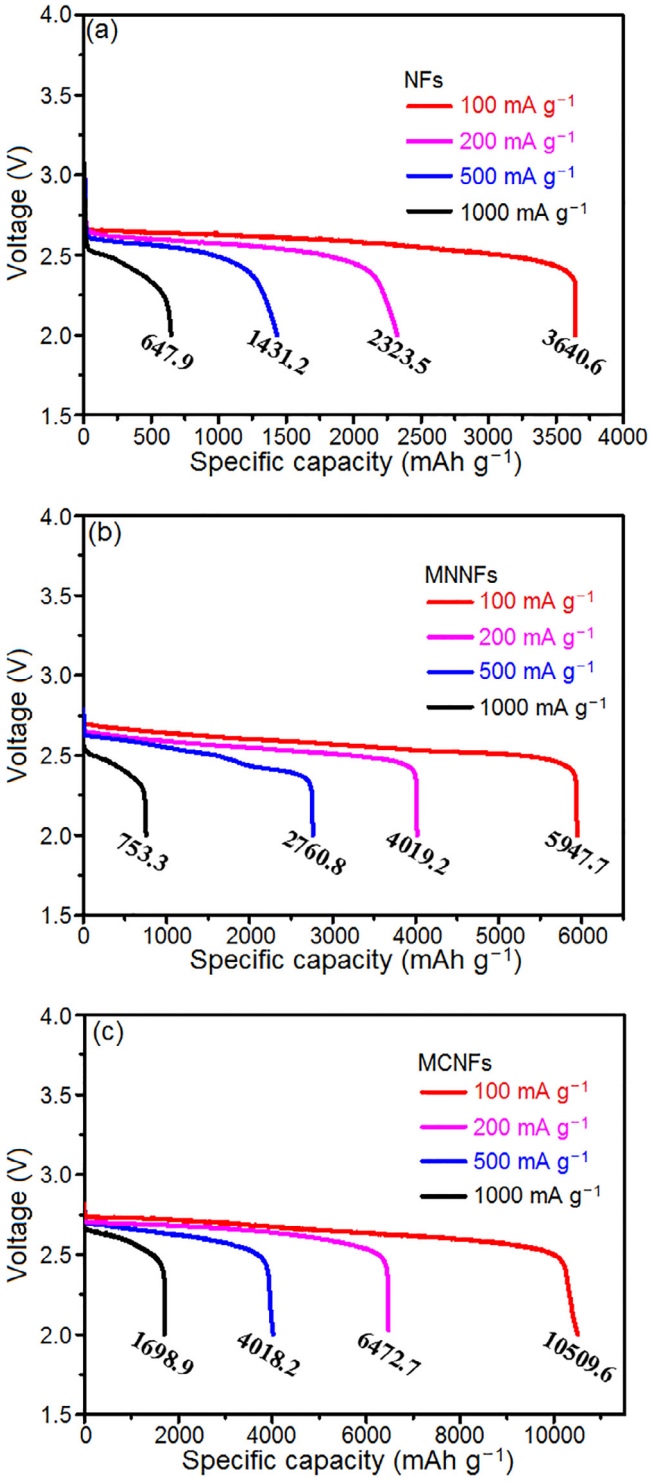

Fig. 5. (Color online) Battery capacity at different densities. The full discharged capacities of the Li-O_2 cells based on NFs (a), MNNFs (b) and MCNFs (c) at different densities.

potential of MCNFs is about 2.77 V, which is obviously lower than that of MNNFs (2.68 V) and NFs (2.68 V). Meanwhile, there are two OER peaks of 3.40 and 3.73 V in the Li-O_2 batteries with MCNFs, corresponding to negative shift than those of MNNFs (3.88 V) and NFs (3.99 V), respectively. All above results reveal that the MCNFs exhibits a higher ORR onset potential, a lower OER onset potential, and a higher ORR/OER peak current compared with that of MNNFs and NFs. These results show that the MCNFs exhibits superior ORR/OER performance towards both the formation and decomposition of discharge product. Encouraged by these results, we have investigated the rate capability of the Li-O_2 batteries with three cathodes at different current densities. As shown in Fig. 4c, the discharge voltage plateau of the MCNFs cathode is higher than that of MNNFs and NFs at a wide variety of current densities. In light of these discoveries, we have carried out full range discharge test of the Li-O_2 batteries with three cathodes at various current densities (Fig. 5). Remarkably, the specific capacity of MCNFs cathode in Li-O_2 battery is 10,509.6 mAh g^{-1} at a current density of 100 mA g^{-1}, which is larger than that of MNNFs cathode (5,947.7 mAh g^{-1}) and NFs cathode (3,640.6 mAh g^{-1}). Even at 1,000 mA g^{-1}, the discharged capacity of MCNFs cathode can still reach 1,698.9 mAh g^{-1}, which is larger than that of MNNFs (753.3 mAh g^{-1}) and NFs (647.9 mAh g^{-1}). To exclude the possible discharge capacity contribution from lithium insertion, the discharge capacity of MCNFs cathode is tested in the Ar atmosphere (Fig. S5 online). It is found that the background discharge capacity of the MCNFs cathode is negligible within the voltage range, suggesting that the discharge capacities of MCNFs cathode are derived from ORR. Eventually, we speculate that the superior electrochemistry performances of the MCNFs cathode are derived from the synergy of the following advantageous factors: (1) the porous and fibrous structure provides sufficient void volume to house the generated discharge products and promote fast mass transfer, (2) good electronic conductivity that enables fast electron transfer from the reaction sites, and (3) good activity of Mo_2C in accelerating the sluggish Li-O_2 reactions.

Another considerable improvement is the cycling stability Li-O_2 battery with MCNFs cathode. These cells were tested with the recently widely used capacity limited cycle method. The cycling performance of Li-O_2 batteries with MCNFs, MNNFs and NFs cathodes was evaluated by galvanostatic cycling at 200 mA g^{-1} with a limited specific capacity of 500 mAh g^{-1}. From Fig. 6, the voltage obtained at the discharge terminal of the Li-O_2 battery with MCNFs cathode in the >2.0 V is 124 cycles. In contrast, the discharge voltages of the MNNFs and NFs degrade to <2.0 V after only 46 and 13 cycles, respectively. Additionally, the Li-O_2 batteries with MCNFs cathodes could live 56 cycles with the specific capacity limit of 1,000 mAh g^{-1} (Fig. S6 online). All above results confirm that MCNFs has superior cycling stability than MNNFs and NFs. To better illustrate the superiority of the MCNFs cathode, a comparison between the cycling performances of our cathode and those of reported Mo_2C or TiC cathode is presented in Table 1. Of note, with the same limited capacity, the cycling performance of the MCNFs cathode tested at 200 mA g^{-1} outperforms that of the MoO_2/Mo_2C@3D NCF, Mo_2C/CNT, TiC-C cathode tested at 100 mA g^{-1}. These results further confirm the excellent cycling stability of MCNFs cathode.

3.3. Mechanism exploration

To understand the reversibility of the MCNFs cathode, the morphology evolution of the discharged and recharged MCNFs cathode are then investigated via SEM, XRD and Raman spectroscopy. As shown in Fig. 7a, after discharging to 1,000 mAh g^{-1} and the current density is 200 mA g^{-1}, sharp peaks at 33°, 35°, 49° and 58°, which correspond to the (1 0 0), (1 0 1), (1 0 3), and (1 1 0) crystal surfaces of Li_2O_2, are observed respectively [37,38]. Additionally, the Raman spectroscopy is carried out to elucidate MCNFs cathode and the chemical bonds that are formed and broken (Fig. 7b). Two bonds of pristine MCNFs at 1325 and 1575 cm^{-1} are, respectively, assigned to the disorder band (D bond) and the graphitic band (G bond) of carbon, where the D bond and the G bond represent the sp^3 C—C single bond and the sp^2 C=C double bond, respectively. After discharge, there are new peaks that appears at 781 and 1,087 cm^{-1}, which represents the formation of Li_2O_2.

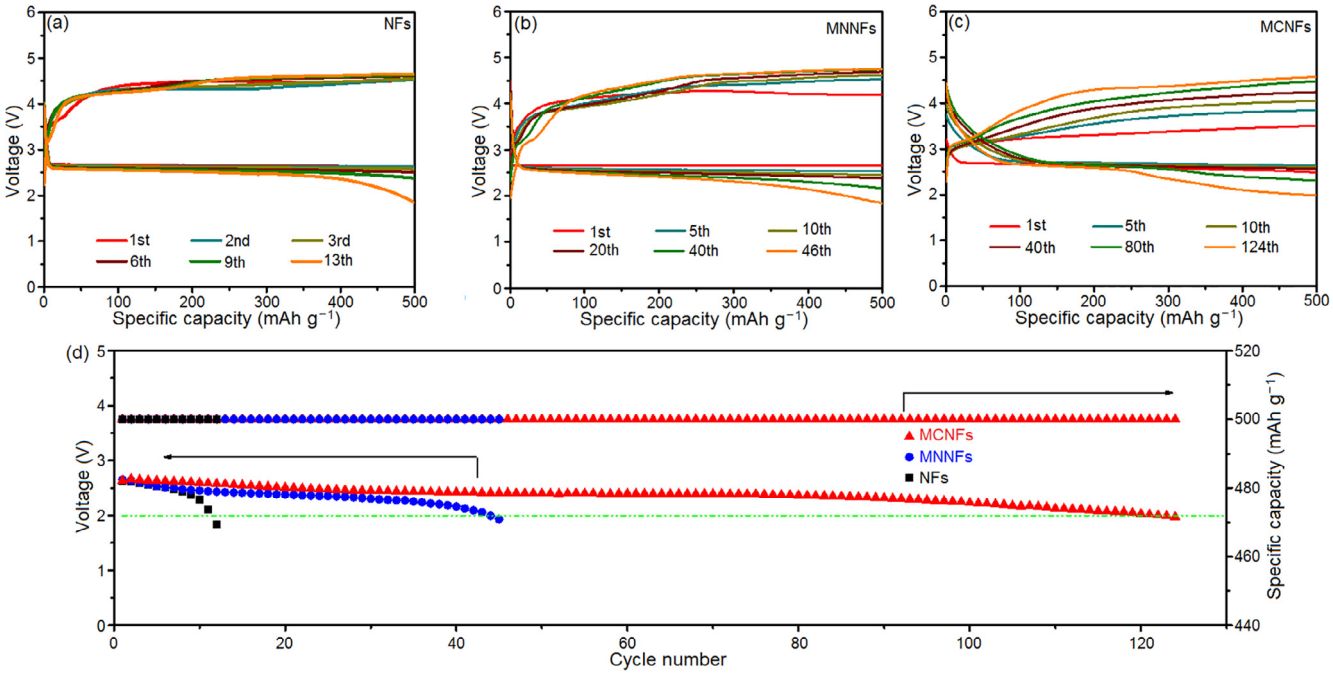

Fig. 6. (Color online) Battery cycling stability. The discharge-charge curves of NFs (a), MNNFs (b) and MCNFs (c) cathode for Li-O_2 battery at a current density of 200 mA g^{-1} with a specific capacity of 500 mAh g^{-1}. (d) The terminal discharge voltage of Li-O_2 batteries with three different cathodes.

Table 1
Comparison of the cycling performances of the MCNFs cathode with those of other reported Mo_2C or TiC based Li-O_2 batteries.

Cathodes	Cycling performance	Measurement conditions	Reference
MCNFs	124 cycles	500 mAh g^{-1} at 200 mA g^{-1}	This work
MoO_2/Mo_2C@3D NCF	120 cycles	500 mAh g^{-1} at 100 mA g^{-1}	[35]
Mo_2C/CNT	100 cycles	500 mAh g^{-1} at 100 mA g^{-1}	[29]
TiC-C	80 cycles	500 mAh g^{-1} at 100 mA g^{-1}	[36]

And these above new peaks in XRD pattern and Raman spectra would dispread after recharged to 1,000 mAh g^{-1} [38,39]. Notably, the morphological changes of the MCNFs cathodes during the electrochemical reaction are shown in Fig. 7c, compared with the clean surface of the MCNFs cathode (Fig. 1c), the toroidal Li_2O_2 crystal uniformly grows along the surface of the MCNFs cathode after discharge [40,41]. After recharge, the toroidal Li_2O_2 crystal disappears and the surface of the cathode becomes smooth again (Fig. 7d), demonstrating a good reversibility of the MCNFs cathodes. And this result is further supported by the electrochemical impedance spectra (EIS) in Fig. S7 (online). It can be found that after the first discharge process, the impedance of the Li-O_2 cell increases significantly, which is due to the poor electronic conductivity of discharge products generated at the cathode side. Interestingly, after subsequent recharging process, the impedance of the Li-O_2 cell could almost recover its initial value, indicating the good rechargeability of the MCNFs cathode. For further understanding the electrochemical behavior in the Li-O_2 battery, the galvanostatic intermittent titration technique (GITT) is also applied (Fig. S8 online). The equilibrium potential of the Li-O_2 battery is near 2.9 V, regardless of the state of discharge, demonstrating the formation of Li_2O_2 [42,43]. In the end, we speculate the mechanism of electrochemical growth of Li_2O_2 based on its morphology. Both theoretical calculations and experiments have demonstrated that the growth of Li_2O_2 during the discharge process could proceed through two different pathways: surface-adsorption pathway and solvation-mediated pathway [44–47]. As shown in Fig. 8, the dissolved Li^+ and O_2 could travel freely in this macroporous structure, and the dissolved O_2 may convert to $LiO_{2(sol)}$ by undergoing a one-electron reduction. Then the dissolved intermediates ultimately form large the toroidal Li_2O_2 crystal with the disproportionation reaction. However, the mechanism of electrochemical growth of Li_2O_2 should be further explored by means of in-situ depth profiling.

4. Conclusion

In conclusion, to fabricate an efficient the cathode for Li-O_2 battery, the MCNFs is designed and fabricated through the electrospinning technology and high temperature treatment. Interestingly, when the MCNFs is applied as the cathode for Li-O_2 battery, superior electrochemical performances, including a high discharge capacity (10,509.6 mAh g^{-1}), a low discharge-charge voltage gap (ca. 1 V), and a long cycle life (up to 124 cycles), are successfully obtained. These results are benefiting from the hierarchically self-standing and binder-free structure of MCNFs with the excellent catalytic properties of the well dispersed Mo_2C nanoparticles. These results suggest that both the material and structure of the cathode should be optimized to simultaneously achieve a superior electrochemical performance of Li-O_2 batteries. We anticipate this strategy could be extended to fabricate others metal carbides materials for the development of high-performing cathode for Li-O_2 battery.

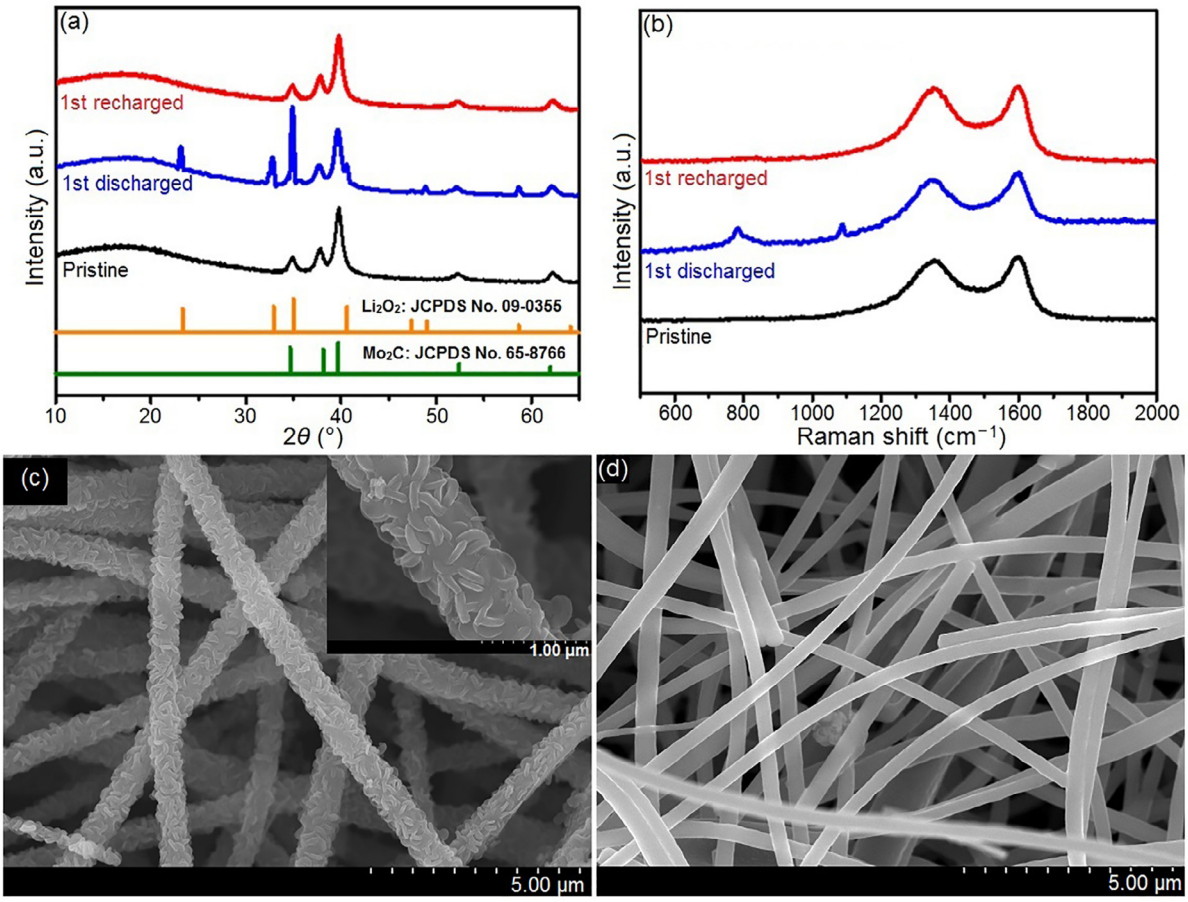

Fig. 7. (Color online) The analysis of discharge product. XRD patterns (a) and Raman spectra (b) of MCNFs cathode at different stages during first cycle. SEM images of the MCNFs cathode after first discharged (c) and recharged (d).

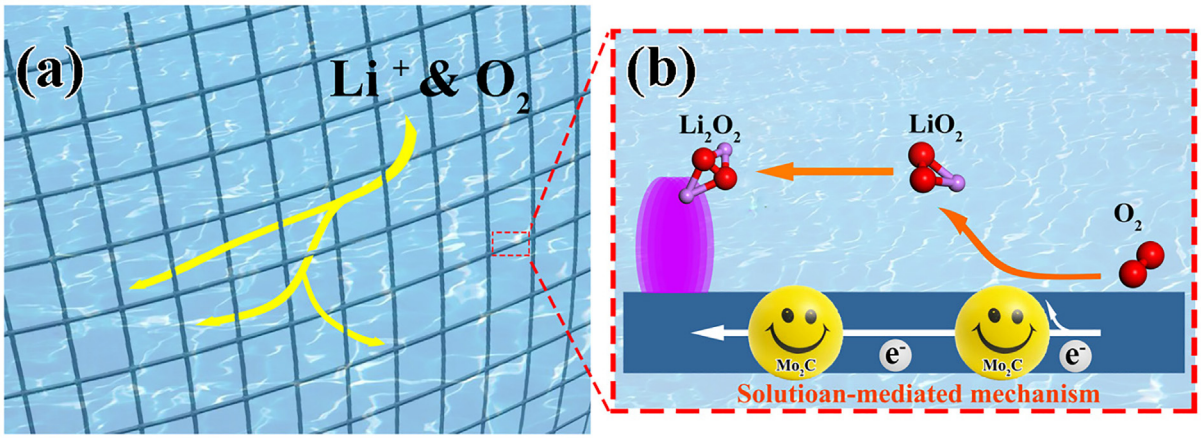

Fig. 8. (Color online) The structure of the oxygen cathode based on MCNFs (a) and the mechanism of electrochemical growth of the toroidal-like Li_2O_2 (b).

Conflict of interest

The authors declare that they have no conflict of interest.

Acknowledgments

This work was supported by the National Key Research and Development Program of China (2017YFA0206704 and 2016YFB0100103), the National Basic Research Program of China (2014CB932300), Strategic Priority Research Program of the Chinese Academy of Sciences (XDA09010404), Technology and Industry for National Defence of China (JCKY2016130B010), the National Natural Science Foundation of China (51771177, 21422108, 51472209, and 51472232), and Jilin Province Science and Technology Development Program (20160101289JC).

Appendix A. Supplementary data

Supplementary data associated with this article can be found, in the online version, at https://doi.org/10.1016/j.scib.2018.02.014.

References

[1] Bruce PG, Freunberger SA, Hardwick LJ, et al. Li-O_2 and Li-S batteries with high energy storage. Nat Mater 2011;11:19–29.
[2] Liu T, Leskes M, Yu WJ, et al. Cycling Li-O_2 batteries via LiOH formation and decomposition. Science 2015;35:530.
[3] Oh SH, Black R, Pomerantseva E, et al. Synthesis of a metallic mesoporous pyrochlore as a catalyst for lithium-O_2 batteries. Nat Chem 2012;4:1004–10.
[4] Xu JJ, Chang ZW, Yin YB, et al. Nanoengineered ultralight and robust all-metal cathode for high-capacity, stable lithium-oxygen batteries. ACS Central Sci 2017;3:598–604.
[5] Zhu J, Wang F, Wang B, et al. Surface acidity as descriptor of catalytic activity for oxygen evolution reaction in Li-O_2 battery. J Am Chem Soc 2015;137:13572–9.
[6] Liu QC, Xu JJ, Yuan S, et al. Artificial protection film on lithium metal anode toward long-cycle-life lithium-oxygen batteries. Adv Mater 2015;27:5241–7.
[7] Hou JB, Yang M, Ellis MW, et al. Lithium oxides precipitation in nonaqueous Li-air batteries. Phys Chem Chem Phys 2012;14:13487–501.
[8] Mitchell RR, Gallant BM, Thompson BM, et al. All-carbon-nanofiber electrodes for high-energy rechargeable Li-O_2 batteries. Energy Environ Sci. 2011;4:2952–8.
[9] Viswanathan V, Thygesen KS, Hummelshøj JS, et al. Electrical conductivity in Li_2O_2 and its role in determining capacity limitations in non-aqueous Li-O_2 batteries. J Chem Phys 2011;135:214704.
[10] Li Z, Robert RM, Yang L, et al. In situ transmission electron microscopy observations of electrochemical oxidation of Li_2O_2. Nano Lett 2013;13:2209–14.
[11] Zhang T, Liao KM, He P, et al. A self-defense redox mediator for efficient lithium-O_2 batteries. Energy Environ Sci 2016;9:1024–30.
[12] Jin L, Xu LP, Morein C, et al. titanium containing γ-MnO_2 (TM) hollow spheres: one-step synthesis and catalytic activities in Li/air batteries and oxidative chemical reactions. Adv Funct Mater 2010;20:3373–82.
[13] Freunberger SA, Chen YH, Drewett NE, et al. The lithium-oxygen battery with ether-based electrolytes. Angew Chem Int Ed 2011;50:8609–13.
[14] Thotiyl MMO, Freunberger SA, Peng ZQC, et al. A stable cathode for the aprotic Li-O_2 battery. Nat Mater 2013;12:1050.
[15] Luo WB, Gao XW, Chou SL, et al. Porous AgPd-Pd composite nanotubes as highly efficient electrocatalysts for lithium-oxygen batteries. Adv Mater 2015;27:6862–9.
[16] Singhal R, Kalra V. Binder-free hierarchically-porous carbon nanofibers decorated with cobalt nanoparticles as efficient cathodes for lithium-oxygen batteries. RSC Adv 2016;6:103072–80.
[17] Xia L, Wang S, Liu G, et al. Flexible SnO_2/N-doped carbon nanofiber films as integrated electrodes for lithium-ion batteries with superior rate capacity and long cycle life. Small 2015;12:853–9.
[18] Tran C, Singhal R, Lawrence D, et al. Polyaniline-coated freestanding porous carbon nanofibers as efficient hybrid electrodes for supercapacitors. J Power Sources 2015;293:373–9.
[19] Ma JL, Meng FL, Xu D, et al. Co-embedded N-doped carbon fibers as highly efficient and binder-free cathode for Na-O_2 batteries. Energy Storage Mater 2017;6:1–8.
[20] Shui JL, Lin Y, Connell JW, et al. Nitrogen-doped holey graphene for high-performance rechargeable Li-O_2 batteries. ACS Energy Lett 2016;1:260–5.
[21] Kim DY, Kim M, Kim DW, et al. Flexible binder-free graphene paper cathodes for high-performance Li-O_2 batteries. Carbon 2015;93:625–35.
[22] Kim JH, Kannan AG, Woo HS, et al. A bi-functional metal-free catalyst composed of dual-doped graphene and mesoporous carbon for rechargeable lithium-oxygen batteries. J Mater Chem A 2015;3:18456–65.
[23] Chen LF, Huang ZH, Liang HW, et al. Flexible all-solid-state high-power supercapacitor fabricated with nitrogen-doped carbon nanofiber electrode material derived from bacterial cellulose. Energy Environ Sci 2013;6:3331–8.
[24] McCloskey BD, Scheffler R, Speidel A, et al. On the efficacy of electrocatalysis in nonaqueous Li-O_2 batteries. J Am Chem Soc 2011;133:18038–41.
[25] Peng ZQ, Freunberger S, Chen Y, et al. A reversible and higher-rate Li-O_2 battery. Science 2012;337:563–6.
[26] Xie J, Yao X, Madden IP, et al. Selective deposition of Ru nanoparticles on $TiSi_2$ nanonet and its utilization for Li_2O_2 formation and decomposition. J Am Chem Soc 2014;136:8903–6.
[27] Liu T, Xu JJ, Liu QC, et al. Ultrathin, lightweight, and wearable Li-O_2 battery with high robustness and gravimetric/volumetric energy density. Small 2017;13:1602952.
[28] Zhang YJ, Li X, Zhang MY, et al. IrO_2 nanoparticles highly dispersed on nitrogen-doped carbon nanotubes as an efficient cathode catalyst for high-performance Li-O_2 batteries. Ceram Int 2017;43:14082–9.
[29] Kwak WJ, Lau KC, Shin CD, et al. A Mo_2C/carbon nanotube composite cathode for lithium-oxygen batteries with high energy efficiency and long cycle life. ACS Nano 2015;9:4129–37.
[30] Kundu D, Black R, Adams B, et al. Nanostructured metal carbides for aprotic Li-O_2 batteries: new insights into interfacial reactions and cathode stability. J Phys Chem Lett 2015;6:2252–8.
[31] Rahaman MS, Ismail AF, Mustafa A. A review of heat treatment on polyacrylonitrile fiber. Polym Degrad Stab 2007;92:1421–32.
[32] Zhao GY, Mo RW, Wang BY, et al. Enhanced cyclability of Li-O_2 batteries based on TiO_2 supported cathodes with no carbon or binder. Chem Mater 2014;26:2551–6.
[33] Gupta P, Elkins C, Long TE, Wilkes GL. Electrospinning of linear homopolymers of poly(methyl methacrylate): exploring relationships between fiber formation, viscosity, molecular weight and concentration in a good solvent. Polymer 2005;46:4799–810.
[34] Li R, Wang S, Wang W, et al. Ultrafine Mo_2C nanoparticles encapsulated in N-doped carbon nanofibers with enhanced lithium storage performance. Phys Chem Chem Phys 2015;38:24803–9.
[35] Lu Y, Ang H, Yan Q, et al. Bioinspired synthesis of hierarchically porous MoO_2/Mo_2C nanocrystal decorated n-doped carbon foam for lithium-oxygen batteries. Chem Mater 2016;28:5743–52.
[36] Qiu FL, He P, Jiang J, et al. Ordered mesoporous TiC-C composites as cathode materials for Li-O_2 batteries. Chem Commun 2016;52:2713–8.
[37] Jian Z, Liu P, Li F, et al. Core-shell-structured CNT@RuO_2 composite as a high-performance cathode catalyst for rechargeable Li-O_2 batteries. Angew Chem Int Ed 2014;53:442–6.
[38] Asadi M, Kumar B, Liu C, et al. Cathode based on molybdenum disulfide nanoflakes for lithium-oxygen batteries. ACS Nano 2016;10:2167–75.
[39] Hu X, Cheng F, Zhang N, et al. Nanocomposite of Fe_2O_3@C@MnO_2 as an Efficient cathode catalyst for rechargeable lithium-oxygen batteries. Small 2015;11:5545–50.
[40] Li FJ, Zhang T, Zhou HS. Challenges of non-aqueous Li-O_2 batteries: electrolytes, catalysts, and anodes. Energy Environ Sci 2013;6:1125–41.
[41] Gao X, Chen Y, Johnson L, et al. Promoting solution phase discharge in Li-O_2 batteries containing weakly solvating electrolyte solutions. Nat Mater 2016;15:882–8.
[42] Lim HK, Lim HD, Park KY, et al. toward a lithium-air battery: the effect of CO_2 on the chemistry of a lithium-oxygen cell. J Am Chem Soc 2013;135:9733–42.
[43] Cui ZH, Gu XX, Li H. Equilibrium voltage and overpotential variation of nonaqueous Li-O_2 batteries using the galvanostatic intermittent titration technique. Energy Environ Sci 2015;8:182–7.
[44] McCloskey BD, Scheffler R, Speidel A, et al. On the mechanism of nonaqueous Li-O_2 electrochemistry on c and its kinetic overpotentials: some implications for Li-air batteries. J Phys Chem C 2012;116:23897–905.
[45] Viswanathan V, Nørskov JK, Speidel A, et al. Li-O_2 kinetic overpotentials: Tafel plots from experiment and first-principles theory. J Phys Chem Lett 2013;4:556–60.
[46] Allen CJ, Hwang J, Kautz R, et al. Oxygen reduction reactions in ionic liquids and the formulation of a general ORR Mechanism for Li-air batteries. J Phys Chem C 2012;116:20755–64.
[47] Xu JJ, Chang ZW, Wang Y, et al. Cathode surface-induced, solvation-mediated, micrometer-sized Li_2O_2 cycling for Li-O_2 batteries. Adv Mater 2016;28:9620–8.

Zhen-Dong Yang graduated from Agricultural University of Hebei Province in 2015. He is currently pursuing a B.S under the supervision of Prof. Jun-min Yan at School of Materials Science and Engineering, Jinlin University. His current interests include the synthesis and characterization of self-standing cathode in lithium-oxygen batteries.

Keke Huang (1979) received his B.C. and Ph.D. in Chemistry from Jilin University at 2002 and 2007, respectively. After graduation, he became a research scientist in State Key Laboratory of Inorganic Synthesis and Preparative Chemistry, Jilin University, Changchun. He was promoted as an associate professor at 2014. He has published over 120 scientific papers in functional inorganic materials. His research interests include design and synthesis new inorganic materials, disproportionation reaction and the relationship of electron state to the physical/chemical performance of inorganic solid state materials.

Xin-Bo Zhang received his Ph.D. degree in inorganic chemistry from Changchun Institute of Applied Chemistry, Chinese Academy of Sciences (CAS) and was granted the CAS Presidential Scholarship Award in 2005. Then, between 2005 and 2010, he worked as a JSPS and NEDO fellow at the National Institute of Advanced Industrial Science and Technology (Kansai Center), Japan. His interests mainly focus on functional inorganic materials for energy storage and conversion with fuel cells and batteries.